On the prediction of martensite formation in metals

E.I. Galindo-Nava

Department of Materials Science and Metallurgy, University of Cambridge

27 Charles Babbage Rd, Cambridge, CB3 0FS, UK

email: eg375@cam.ac.uk, +44 1223 334371

Abstract

A new approach to predict athermal martensite formation in metals is presented. It is based on computing the driving force of the transformation including a strain energy term induced by atomic shear displacements and energy terms due to substitutional and interstitial lattice distortions. The model is applied to prescribe the martensite and austenite start temperatures in Fe–, Ti– and Co–based alloys with no adjustable parameters. Expressions for M_s variations with composition are derived for multicomponent systems. The transformation temperature hysteresis is predicted in Co alloys showing that this approximation can be used to design alloys with the shape memory effect.

Keywords: 4. martensitic phase transformation; 3. Martensitic steels; 3. Shape memory alloys; 3. Titanium alloys; 5. CALPHAD

Martensitic transformations have been studied extensively due to their importance in applications for high–strength, shape–memory effects or superelastic properties. These are diffusionless first order solid–state transformations, which nucleate from a parent phase, commonly referred to as austenite. Martensite nucleates at a critical temperature M_s (martensite–start) when the driving force for its nucleation is reached. Additional undercooling is required for the transformation to continue and reach completion at a temperature M_f (Martensite–finish). The reverse transition occurs upon heating the martensite to transform back to austenite; the temperatures at which the transformation begins and finish are austenite start

(A_s) and finish (A_f), respectively. Although there are considerable studies in different alloying systems showing how martensite formation changes with composition [1–4], there is virtually no theoretical approximation able to predict the conditions for its occurrence without introducing fitting parameters or remaining valid in different phase transitions.

The objective of this work is to introduce a new approach to predict M_s in systems undergoing the phase transitions: face–centred cubic (FCC)⇔body–centred cubic (BCC), FCC⇔hexagonal closed packed (HCP) and BCC⇒HCP. The approach is based on determining the driving force for athermal martensite formation including energy terms of the transformation strains and lattice distortions by substitutional and interstitial atoms. The model has no adjustable parameters and it is able to predict M_s and A_s in Fe–, Ti–based alloys, as well as the hysteresis cycle (M_s, M_f, A_s, A_f) in Co–based alloys.

Martensite forms by the coordinated movement of atoms resulting in homogeneous shearing of the austenite and forming a new crystal structure without variations in chemical composition. The lattice correspondence between the austenite and martensite phases are nearly parallel to the most densely packed planes and their corresponding directions. This leads to the orientation relationships between the FCC, BCC, and HCP phase transitions to be*: $\{111\}_{\mathrm{FCC}}||\{110\}_{\mathrm{BCC}}||\{0001\}_{\mathrm{HCP}}$ and $\langle 110\rangle_{\mathrm{FCC}}||\langle 111\rangle_{\mathrm{BCC}}||\langle 11\bar{2}0\rangle_{\mathrm{HCP}}$.

The phenomenological theory of martensite crystallography dictates that the transformation strain γ_T consists of two components; a (Bain) strain distorting homogeneously the parent structure, and a lattice invariant strain δ aiding in producing the correct shape of the martensitic structure. For the FCC⇒BCC transition the transformation strain is computed by rotating the FCC unit cell, expanding two principal axes and compressing the remaining axis to correspond with the BCC unit cell [8]. Additional shearing of $\delta = \frac{|\sqrt{2}a_\gamma - \sqrt{3}a_{\alpha'}|}{a_\gamma}$ along $\langle\bar{1}10\rangle_{\mathrm{FCC}}$ is needed to achieve the correct shape. This is illustrated in Figure 1(a), showing atoms in $(111)_{\mathrm{FCC}}||(110)_{\mathrm{BCC}}$ (red) shuffle by $\frac{\delta a_\gamma}{\sqrt{2}}[\bar{1}10]_{\mathrm{FCC}}$ (orange arrows) to reach the cor-

*These are idealised relations, however they have shown sufficient accuracy with experiments when determining various crystallographic parameters [5–7].

rect BCC shape (green). The principal strains to compute γ_T are [8]: $\eta_1 = \frac{\frac{1}{\sqrt{2}}a_\gamma(1-\frac{\delta}{\sqrt{2}})-a_{\alpha'}}{\frac{1}{\sqrt{2}}a_\gamma(1-\frac{\delta}{\sqrt{2}})}$, $\eta_2 = \frac{\frac{1}{\sqrt{2}}a_\gamma(1+\frac{\delta}{\sqrt{2}})-a_{\alpha'}}{\frac{1}{\sqrt{2}}a_\gamma(1+\frac{\delta}{\sqrt{2}})}$ and $\eta_3 = \frac{\frac{1}{\sqrt{2}}a_\gamma-a_{\alpha'}}{\frac{1}{\sqrt{2}}a_\gamma}$. The transformation strain is: $\gamma_T = \sqrt{\eta_1^2+\eta_2^2+\eta_3^2}$. The principal strains of the BCC⇒FCC transition are computed by similar rotations and by shearing $\frac{\delta a_{\alpha'}}{\sqrt{3}}[1\bar{1}1]_{\rm BCC}$ the lattice, with $\delta = \frac{|\sqrt{2}a_\gamma-\sqrt{3}a_{\alpha'}|}{a_{\alpha'}}$.

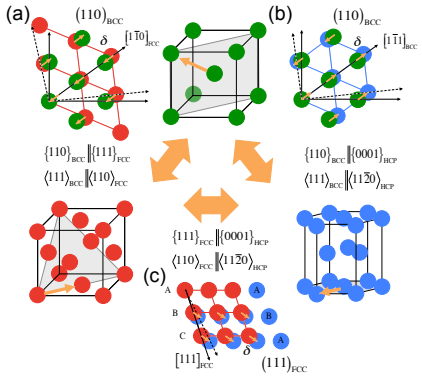

Figure 1: Schematic representation of the atomic displacements in BCC⇔FCC, FCC⇔HCP and BCC⇔HCP transitions and their orientation relationships.

Burgers [9] followed a similar argument to compute γ_T in the BCC⇒HCP transition. This is illustrated in Figure 1(b), where BCC atoms shear $\delta = \frac{|\sqrt{3}a_\beta-2a_\alpha|}{a_\beta}$ along $\langle 111\rangle_{\rm BCC}$ to achieve the correct shape of the HCP lattice (blue atoms). The shifting of $\frac{\delta a_{\alpha'}}{\sqrt{3}}[1\bar{1}1]_{\rm BCC}$ in the BCC axes is included in the computation of the principal (Bain) strains [10].

The FCC⇒HCP transformation strain is obtained by shearing atoms $\delta = \frac{1}{6}\langle 11\bar{2}\rangle$ [11–14]. Two of the principal strains (η_1 and η_2) are obtained by rotating and expanding $[100]_{\rm FCC}$ and $[010]_{\rm FCC}$ in correspondence with $[10\bar{1}0]_{\rm HCP}$ and $[11\bar{2}0]_{\rm HCP}$ [14]. As for η_3, the $[111]_{\rm FCC}$ axis is expanded by δ to lie parallel to $[0001]_{\rm HCP}$, as schematically shown in Figure 1(c) (orange arrows). This results in its magnitude increasing to $a_\gamma\sqrt{(1+\frac{1}{6})^2+(1+\frac{1}{6})^2+(1-\frac{2}{6})^2} = a_\gamma\sqrt{\frac{19}{6}}$ and η_3 is [14]: $\eta_3 = \frac{\frac{2}{3}\sqrt{\frac{19}{6}}a_\gamma-c_\epsilon}{\frac{2}{3}\sqrt{\frac{19}{6}}a_\gamma}$. The HCP⇒FCC transition has been argued to occur by the reverse process with analogous principal strains [13, 14].

Table 1 shows the values of the principal strains and the resulting transformation strains.

The lattice constants have been obtained from [7, 15–18]; these are for Fe $a_\gamma = 0.357$ nm and $a_\alpha = 0.287$ nm; for Ti, $a_\beta = 0.328$ nm, $a_\alpha = 0.295$ nm and $c_\alpha = 0.468$ nm; and for Co, $a_\gamma = 0.35$ nm, $a_\epsilon = 0.25$ nm and $c_\epsilon = 0.406$ nm.

Table 1: Transformation strain and ΔG_T in different phase transitions.

Transition	η_1	η_2	η_3	γ_T	$\lvert\Delta G_T\rvert$ (J/mol)	Exp (J/mol)
FCC⇒BCC	$\frac{\frac{1}{\sqrt{2}}a_\gamma(1+\frac{\delta}{\sqrt{2}})-a_{\alpha'}}{\frac{1}{\sqrt{2}}a_\gamma(1+\frac{\delta}{\sqrt{2}})}$	$\frac{\frac{1}{\sqrt{2}}a_\gamma(1-\frac{\delta}{\sqrt{2}})-a_{\alpha'}}{\frac{1}{\sqrt{2}}a_\gamma(1-\frac{\delta}{\sqrt{2}})}$	$\frac{\frac{1}{\sqrt{2}}a_\gamma-a_{\alpha'}}{\frac{1}{\sqrt{2}}a_\gamma}$	0.24 (Fe)	1255	1000–1250 [19–21]
BCC⇒FCC	$\frac{a_{\alpha'}(1+\frac{\delta}{\sqrt{3}})-\frac{\sqrt{2}}{2}a_\gamma}{a_{\alpha'}(1+\frac{\delta}{\sqrt{3}})}$	$\frac{\sqrt{2}a_{\alpha'}(1-\frac{\delta}{\sqrt{3}})-\sqrt{\frac{3}{2}}a_\gamma}{\sqrt{2}a_{\alpha'}(1-\frac{\delta}{\sqrt{3}})}$	$\frac{\sqrt{2}a_{\alpha'}(1+\frac{\delta}{\sqrt{3}})-\sqrt{\frac{3}{2}}a_\gamma}{\sqrt{2}a_{\alpha'}(1+\frac{\delta}{\sqrt{3}})}$	0.17 (Fe)	500	
BCC⇒HCP	$\frac{(1+\frac{\delta}{\sqrt{3}})a_\beta-a_{\alpha'}}{(1+\frac{\delta}{\sqrt{3}})a_\beta}$	$\frac{(1-\frac{\delta}{\sqrt{3}})\sqrt{2}a_\beta-\sqrt{3}a_{\alpha'}}{(1-\frac{\delta}{\sqrt{3}})\sqrt{2}a_\beta}$	$\frac{(1+\frac{\delta}{\sqrt{3}})\sqrt{2}a_\beta-c_{\alpha'}}{(1+\frac{\delta}{\sqrt{3}})\sqrt{2}a_\beta}$	0.1014 (Ti)	130	150 [3]
FCC⇒HCP	$\frac{\frac{1}{\sqrt{2}}a_\gamma-a_\varepsilon}{\frac{1}{\sqrt{2}}a_\gamma}$	$\frac{\frac{1}{\sqrt{2}}a_\gamma-a_\varepsilon}{\frac{1}{\sqrt{2}}a_\gamma}$	$\frac{\frac{2}{3}\sqrt{\frac{19}{6}}a_\gamma-c_\varepsilon}{\frac{2}{3}\sqrt{\frac{19}{6}}a_\gamma}$	0.026 (Co)	18	35 [22]
HCP⇒FCC	$\frac{\sqrt{2}a_\varepsilon-a_\gamma}{\sqrt{2}a_\varepsilon}$	$\frac{\sqrt{2}a_\varepsilon-a_\gamma}{\sqrt{2}a_\varepsilon}$	$\frac{c_\varepsilon-\frac{2}{3}\sqrt{\frac{19}{6}}a_\gamma}{c_\varepsilon}$	0.027 (Co)	18.8	

The chemical driving force for athermal martensite, $\Delta G^{\gamma\Rightarrow\alpha'}$, is the difference of the Gibbs energy between the austenite and the martensite. $\Delta G^{\gamma\Rightarrow\alpha'}$ has been the subject of extensive investigations in binary and multicomponent alloys combining the CALPHAD (Calculation of phase diagrams) approach and experimental data [21,23,24]; in this context, martensite is treated as supersaturated ferrite in Fe [24], and supersaturated α in Ti and Zr [7]. $\Delta G^{\gamma\Rightarrow\alpha'}$ has been rationalised as the sum of the strain energy resulting from the lattice distortions accompanying the transformation, ΔG_T, and distortions in the lattice produced by substitutional, ΔG_{subs}, and/or interstitial atoms, ΔG_{int}. If thermal activation is not considered $\Delta G_{Ms}^{\gamma\Rightarrow\alpha'}$ is [25,26]:

$$\Delta G_{Ms}^{\gamma\Rightarrow\alpha'} = \Delta G_T + \Delta G_{subs} + \Delta G_{int}. \tag{1}$$

ΔG_T can be considered as the elastic strain energy in a (atomic–scale) region undergoing shape changes; such energy has been estimated by Eshelby [27]. His approach is based on determining the pressure induced by inserting an inclusion within an isotropic matrix and

the strain energy equals:

$$E_{strain} = -\frac{2}{9}\frac{(1+\nu)}{(1-\nu)}\mu\Delta V\varepsilon^2, \tag{2}$$

where μ is the shear modulus, ν is the Poisson's ratio, ΔV is the volume under deformation and ε is the dilatational strain. Equation 2 is employed to estimate the strain energy produced by local atomic displacements. ΔV is proportional to the molar volume of the principal component [8]: $\Delta V = \frac{1}{2}V_m$, where the $\frac{1}{2}$ term accounts for the effective volume expansion occurring in a shear plane [28]. The dilatational strain can be related to γ_T using the Schmidt relation in a single crystal [29], $\varepsilon = \frac{1}{2}\gamma_T$, as the shear transformation follows the closest–packed directions. Combining these results, ΔG_T is:

$$\Delta G_T = -\frac{(1+\nu)\mu V_m}{36(1-\nu)}\gamma_T^2. \tag{3}$$

This equation depends only on the magnitude of γ_T, and it can be applied to different metallic systems. Table 1 shows the magnitude of ΔG_T computed at M_s in FCC⇔BCC for Fe, BCC⇒HCP for Ti and FCC⇔HCP for Co. V_m and ν have been obtained from [30]; in Fe, these are 7.09 cm^3/mol and 0.29, respectively; for Ti, V_m = 10.64 cm^3/mol and ν =0.32; and for Co, V_m = 6.6 cm^3/mol and ν = 0.31. Temperature and composition also affect the driving force via the shear modulus. For Fe, $\mu = \left(8.068 + \sum_i \frac{d\mu}{dx_i}x_i\right)\left(1 - 0.48797(\frac{T}{T_C})^2 + 0.12651\left(\frac{T}{T_C}\right)^3\right) \times 10^{10}$ Pa, was obtained from [31], where T_C = 1043 K is the Curie temperature, and $\frac{d\mu}{dx_i}$ are constants dictating the contribution of element i to μ; values of different elements can be found in [31]. In Ti, μ variations with temperature were obtained from Young moduli measurements in [32]: $\mu = \frac{1}{2(1+\nu)}(119.4 - 0.07193(T - 273))$ GPa, whereas for Co, $\mu = \frac{3(1-2\nu)}{2(1+\nu)}(19.509 - 0.001T - 3\times10^{-6}T^2)\times10^{10}$ Pa is computed from Bulk moduli measurements in [33]. No systematic reports for μ variations with composition in Ti or Co were found in the literature, thus normalised linear mixtures with composition were adopted, as suggested in [34]: $\frac{1}{\mu}\left(\mu + \sum_i(\mu_i - \mu)x_i\right)$, where μ is the modulus of Ti or

Co, and μ_i is the modulus of element i obtained from [30]. The model predictions are in very good agreement with reported experimental estimations (also shown in Table 1). For the FCC⇒HCP transformation, Cotes, *et al.* [22] have fitted $|\Delta G_T^{\gamma\Rightarrow\epsilon}|$ in $\gamma-$Fe to be $\sim$ 35 J/mol[†]; the elastic and lattice constants of $\gamma-$Fe and Co are similar, thus $|\Delta G_T|$ in Co should have the same order of magnitude. These results demonstrate that equation 3 successfully predicts the driving force for martensite nucleation in pure elements using γ_T as input.

Eshelby has also derived an expression for the elastic strain energy resulting from random distributions of solute atoms embedded within the matrix [35]: $-\frac{2}{9}\frac{(1+\nu)}{(1-\nu)}\mu\Delta V_i\varepsilon_i^2 x_i$, where x_i is the atom fraction of alloying element i, ε_i is the strain induced by solute atom i and ΔV_i is the distorted volume. The dilatation strain produced by substitutional atoms is given by the difference between atomic radii [36]: $\varepsilon_i = \frac{r_a - r_{a,i}}{r_a}$, where r_a is the atomic radius of the main component and $r_{a,i}$ is the atomic radius of element i. The strain induced by interstitial atoms depends on their location in the lattice. For instance, C and N atoms prefer to occupy the octahedral sites in the BCC lattice of Fe. The strain induced by an interstitial atom in Fe is estimated as the difference between the largest atom radius fitting in an octahedral site without distorting the lattice, $0.15r_a$ [8], and the radius of C or N: $\varepsilon_j = \frac{r_{a,j} - 0.15r_a}{0.15r_a}$, where j =C, N.

ΔV_i for substitutional atoms is approximated by the volume of a replaced atom, $\left(\frac{4}{3}\pi r_a^3 N_a\right)$, whereas for interstitial atoms it represents the dilatation volume of occupied interstitial sites, $\left(\frac{4}{3}\pi r_{a,j}^3 N_a\right)$. Additionally, when both substitutional and interstitial atoms are added they will likely interact, due variations in the local atomic radii in the lattice [37,38], therefore inducing a second–order component in the lattice distortion energy. If C and N are considered in the BCC lattice, there are 12 possible interstitial sites having the smallest interstices ($0.15r_a$) between atoms in a unit cell, whereas there are 8 possible sites for substitutional atoms to lie adjacent to these interstitial sites, thus there are $12 \times 8 = 96$ possible combinations for

[†]The authors estimated the driving force in Fe–Mn–Si and this value represents the extrapolation of ΔG_T to γ–Fe.

a substitutional atom to interact with an interstitial atom within an unit cell. $\Delta V_{j,i}$ in this case will be considered as the product of the dilatation volume of an interstitial atom and the possible configurations for an interstitial to interact with a substitutional with concentration x_i: $\Delta V_{j,i} = 96x_i\left(\frac{4}{3}\pi r_{a,j}^3 N_a\right)$. The lattice strain is similar to the one for pure interstitial distortions (ε_j), however considering a substitutional atom adjacent to an octahedral site: $\varepsilon_{j,i} = \frac{r_{a,j}-(0.65r_a-0.5r_{a,i})}{(0.65r_a-0.5r_{a,i})}$. Second–order interactions between substitutional atoms of different species are also possible, but they will not be considered in this work and multicomponent alloys with relatively low solute concentrations are explored only. This can be extended in future work.

The previous analysis is extended to multicomponent systems by considering linear combinations of the strain energies in different substitutional/interstitial elements. This is possible if it is assumed that they do not interact, as Eshelby's description is based on non–interacting point defects [35]. The resulting strain energies due to alloying additions in multicomponent alloys are:

$$\begin{aligned}
\Delta G_{subs} &= -\frac{8\pi(1+\nu)}{27(1-\nu)} r_a^3 \mu N_a \sum_i \varepsilon_i^2 x_i \\
\Delta G_{int} &= -\frac{8\pi(1+\nu)}{27(1-\nu)} \mu N_a \sum_j r_j^3 \varepsilon_j^2 x_j - \frac{768\pi(1+\nu)}{27(1-\nu)} \mu N_a \left(\sum_{i,j} r_j^3 \varepsilon_{j,i}^2 x_i x_j \right),
\end{aligned} \tag{4}$$

The driving force at M_s in different alloys can be obtained combining equations 3 and 4. Figure 2(a) shows the model predictions (lines) and experimental data (points) of M_s in Fe–X (X=Ni, Mn, Cr, Co); additional results for A_s in Fe–Mn are shown in the figure (dashed line). The experimental data were obtained from [1, 24, 39]. The thermodynamic software Thermocalc is employed to compute $\Delta G^{\gamma \Rightarrow \alpha'}$ using TCFe8, a commercial database released by Thermo-Calc Software AB and it includes thermodynamic data for multi-component systems of steels/Fe–alloys. The free energy of martensite is considered as supersaturated ferrite in agreement with previous studies using the CALPHAD approach [24]. The values of the

atomic radii have been obtained from [30]. M_s is obtained when $\Delta G^{\gamma \Rightarrow \alpha'}$ equals equation 1, whereas for A_s the driving force $\Delta G^{\alpha' \Rightarrow \gamma}$ is considered. MATLAB scripts for computing the driving force in the systems under study are included as supplementary material. The model agreement with experiments is remarkable in both cases, as the predictions differ only by up to ±50 °C for the conditions tested. However, M_s in Fe–Mn are more scattered. This can be due to the possible formation of (HCP) ϵ–martensite occurring at higher manganese contents and lowering the transformation temperature [39] or due to a different solid solution exponent in equation 4. Figure 2(b) shows additional results for M_s in Fe–C (blue) and Fe–N (red) along with experimental data for Fe–C obtained from [5, 40]; the model shows very good agreement for the compositional range under consideration, as the predictions lie within ±30 °C of experiments, although M_s predictions in Fe–C are slightly lower with C$\geq$ 0.6 wt%; this can be due to transitions in martensite morphology from laths to plates [5]. Additional results in the Fe–Si–C system are shown in order to highlight second–order effects described by equation 4. Experimental data obtained from [41–45] are also shown (dots) for Si additions of 1 (green), 1.5 (orange) and 2 (violet) wt%[‡]. The model shows very good results, confirming second–order interactions between Si and C, as the slope of M_s with increasing carbon changes when increasing Si content. Other authors have reported similar slope variations in Fe-Cr-C [24].

[‡]In some cases the experiments contain other alloying additions, such as Cr and Mn, and the experimental M_s is extrapolated by removing the alloying effects of these elements using the results from (a).

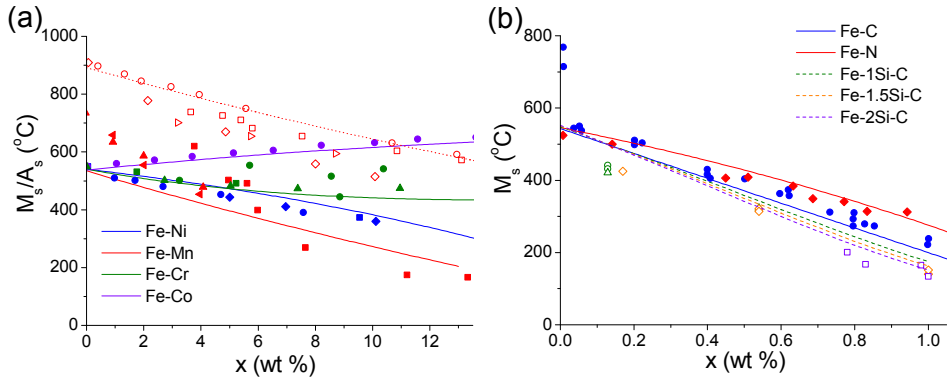

Figure 2: M_s/A_s variation with composition in steels with (a) substitutional and (c) interstitial alloying elements.

Figure 3(a) shows M_s predictions and experimental results in Ti–X (X=Fe, V, Mo, Nb, Zr) obtained from [3, 7, 46, 47]. TTTi3 database is used to obtain the driving force for BCC⇒HCP, $\Delta G^{\beta\Rightarrow\alpha}$; this is a commercial database optimised for multi-component Ti–based alloys and it has been released by Thermotech Ltd. The model shows excellent agreement in all cases, although in Ti-Fe and Ti-V the predicted M_s is higher than the experimental data when Fe$\geq$ 3 wt% and V$\geq$ 7 wt%, respectively. This can be due to different solid solution exponents in equation 4 for these elements or due to deviations in the computed free energies; for instance, the BCC phase in Ti–V is not stable in equilibrium when $V \geq 3$ wt% [7].

In order to show that the model does not depend of the database choice, additional calculations in both ends of Fe-Ti and Co–Fe have been performed using SSOL5, a commercial database produced by the Scientific Group Thermodata Europe, which includes thermodynamic databases for many binary and ternary alloys. Fig 3(b) shows M_s predictions using SSOL5 (solid) and predictions using databases optimised for Fe, Ti and Co alloys (dotted). TCNi8 is used for Co; this is a commercial database optimised for superalloys, including Co–rich alloys, and it has been released by Thermo-Calc Software AB. For Fe-Ti, the calculations were computed up to Ti=1.5 wt%, as this is the limit for austenite formation [48]. The predictions using different databases are practically identical, showing that the model is

consistent, irrespective of the database choice.

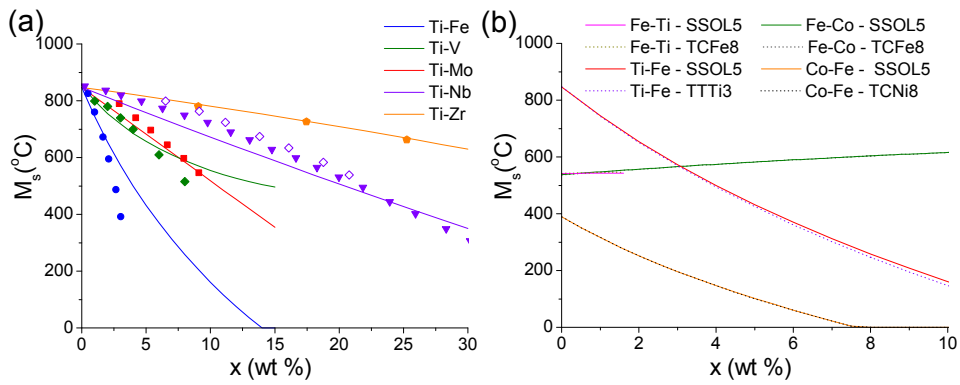

Figure 3: (a) M_s variation with composition in binary Ti alloys. (b) Comparison of M_s predictions in Fe-Ti and Fe-Co using different thermodynamic databases.

These results showed that it is possible to predict M_s if the driving force is known using the CALPHAD approach. However, in practice in multicomponent systems it is more efficient to predict M_s using their nominal composition only. M_s predictions for Fe and Ti (Figs. 2 and 3) are fitted to polynomial approximations as a function of the alloying content (in wt%). Additional calculations are performed in Fe–X–C with X=Ni, Mn, Cr, Co, Si, Mo, Ti, each element up to 5 wt% or the γ–formation limit, and C$\leq$ 0.5 wt%, and in Ti–Cr with Cr$\leq$ 10 wt%, giving:

$$\begin{aligned} M_s^{\mathrm{Fe}} &= 543 - (347\mathrm{C} - 4\mathrm{C}^2) - (10.4\mathrm{Ni} + 0.5\mathrm{Ni}^2) - (28.8\mathrm{Mn} - 0.26\mathrm{Mn}^2) + (9.7\mathrm{Co} - 0.2\mathrm{Co}^2) \\ &\quad -(15.5\mathrm{Cr} - 0.58\mathrm{Cr}^2) + (4\mathrm{Si} - 0.22\mathrm{Si}^2) - (1.3\mathrm{Mo} + 0.3\mathrm{Mo}^2) + (4\mathrm{Ti} - 0.38\mathrm{Ti}^2) \\ &\quad -\mathrm{C}\big(27\mathrm{Ni} + 27\mathrm{Mn} + 20\mathrm{Co} + 15\mathrm{Cr} + 35\mathrm{Si} + 12\mathrm{Mo} + 90\mathrm{Ti}\big) \\ M_s^{\mathrm{Ti}} &= 840 - (95\mathrm{Fe} - 2.5\mathrm{Fe}^2) - (42.5\mathrm{V} - 1.3\mathrm{V}^2) - (32.8\mathrm{Mo} - 0.0015\mathrm{Mo}^2) \\ &\quad -(18\mathrm{Nb} - 0.048\mathrm{Nb}^2) - (6.2\mathrm{Zr} + 0.032\mathrm{Zr}^2) - (51\mathrm{Cr} - 1.9\mathrm{Cr}^2) \end{aligned} \quad (5)$$

The linear coefficients for steels are very close to values fitted by other authors in low–

alloy steels [2]. Moreover, the present predictions are expected to be more accurate, as second–order interactions between C and substitutional atoms are included. For instance, the experimental M_s in 53 steels reported in [43] were reproduced using equation 5 obtaining a correlation coefficient of $R^2 = 0.95$. However, equation 5 may not be valid for higher alloying content.

The martensite finish temperature upon further cooling has been rationalised as the point where the strain energy from the transformation is fully released [49,50]. In cobalt alloys, the transformation is generally accepted to be crystallographically reversible and symmetric [4, 13], as $|\Delta G^{\gamma\Rightarrow\epsilon}| \approx |\Delta G^{\epsilon\Rightarrow\gamma}|$. This implies that the driving force at M_f includes an additional ΔG_T term in $\Delta G_{Ms}^{\gamma\overset{\Rightarrow}{\epsilon}}$, in order to release the transformation energy at M_s [22, 51], *i.e.*:

$$\Delta G_{Mf}^{\gamma\overset{\Rightarrow}{\epsilon}} = \Delta G_{Ms}^{\gamma\overset{\Rightarrow}{\epsilon}} + \Delta G_T = 2\Delta G_T + \Delta G_{subs} + \Delta G_{int}. \tag{6}$$

A similar argument is followed for the driving force of A_f to lead: $\Delta G_{Af}^{\epsilon\overset{\Rightarrow}{\gamma}} = \Delta G_{As}^{\epsilon\overset{\Rightarrow}{\gamma}} + \Delta G_T$. Figure 4 shows the model predictions and experimental data for M_s, M_f, A_s and A_f in Co–X (X=Si, Ni, C) undergoing FCC⇔HCP ($\gamma \Leftrightarrow \epsilon$) transitions; experiments were obtained from [52–54]; C is assumed to occupy octahedral sites in the FCC lattice, hence $\varepsilon_{\mathrm{C}} \approx \frac{r_{a,\mathrm{C}} - 0.41 r_{a,\mathrm{Co}}}{0.41 r_{a,\mathrm{Co}}}$ [8]. The TCNi8 database is used for the calculations. The model has good agreement in all cases, showing that it is able to predict the transformation temperature hysteresis, with discrepancies up to 50°C.

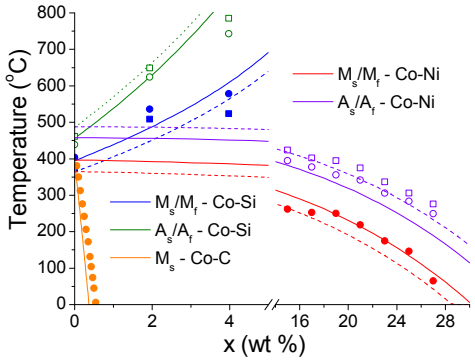

Figure 4: Transformation temperature hysteresis in Co–based alloys with alloying content. The solid lines represent the predicted M_s/A_s, whereas the dashed lines represent M_f/A_f. The solid points represent experimental M_s/M_f, whereas the open points are A_s/A_f.

The model reproduced well the experimental trends of A_f, however a generalised description of the kinetics of this process in other alloys may require more in-depth analysis. The linear and symmetric approximation for the driving force in A_f (equation 6) is based on having low and similar values of the transformation strains between FCC⇒HCP and HCP⇒FCC (Table 1). However, in Fe the lattice strain of FCC⇒BCC and BCC⇒FCC are significantly different, therefore the strain accommodated by austenite formation will not be enough to finish the transformation process and other effects, such as geometric partitioning, morphology and thermal activation, would affect the kinetics to reach A_f. Nevertheless, Liu *et al.* [55] have shown that the HCP⇒FCC transformation is crystallographically reversible, in the way that for temperatures at and above A_f the martensite always returns to the FCC crystal structure upon the reverse transformation and not all the martensite structure is fully dissolved. They also observed shape changes and residual stacking faults indicating that the process is not mechanically reversible. The current approach for A_f in Co does not contradict these results, as it describes the temperature at which the austenite finish transforming but does not disregard the possibility of having residual crystal defects or retained HCP due to the autocatalytic nature of martensite.

The model is valid, in principle, for M_s above room temperature, as athermal effects in the driving force have been considered only. Ghosh and Olson [25, 26] have argued thermal and athermal contributions can alter the driving force, however thermal effects are negligible for M_s above room temperature. The model was shown valid in steels with substitutional and interstitial additions up to 13 wt% (or the limit for austenite formation) and 0.6 wt%, respectively; and in binary Ti–X for Zr and Nb additions up to 14 wt% and for Mo, and V additions up to 10 wt%; above these ranges the martensite morphology may change and twins can also form [5, 7]. For Co, it was valid for Ni and Si content where no twins are present [52,53,55]. In addition, the model was not very accurate in various systems, including Fe–Mn, Ti–Fe, and Ti–V, and the predictions could be improved by modifying the exponent of the solid solution approximation. Existing approaches by Neelakantan *et al.* [3] and Ghosh and Olson [25] incorporated compositional effects in the same form of solid solution hardening by slip deformation. They used exponents of $x_i^{1.5}$ and $\mathrm{x}_i^{0.5}$, respectively, to fit the driving forces of Ti and Fe alloys, whereas in the present case linear variations were considered. Their models were accurate, however the coefficients they obtained are empirical and could not be correlated with the lattice distortions induced by different elements. Moreover, Ghosh and Olson did not find clear correspondence between the effect of a solute in the driving force and its solid solution hardening effect by slip. In contrast, the current approach does not involve fitting parameters, as the solid solution coefficients are expressed in terms of the lattice distortion strain produced by each element and the same approximation is valid irrespective of the system, *e.g.* the approach was successful in predicting M_s in Fe–C (Fig. 2(b)) and Co-C (Fig 4(a)).

The approximation is restricted to systems undergoing the FCC⇔BCC⇔HCP transitions and additional work is required to account for other phases, variations in martensite morphology and formation of other crystal defects; these features would modify the approach by adding frictional terms in the driving force due to thermal activation, shape changes, forest

hardening and/or twin formation. These modifications can be done in future work.

An analytic approach was defined to predict M_s in metals. The model was validated in different alloying systems showing that compositional effects not only affect the chemical driving force, but they also contribute to increasing the net lattice distortions. Complete transformation temperature hysteresis was predicted in Co–based alloys by only modifying the underlying transformation strains, showing that the model could aid in designing alloys with shape memory effects.

Acknowledgements

The author would like to acknowledge the Royal Academy of Engineering for his research fellowship funding and to Prof. Mark Blamire for the provision of laboratory facilities.

References

[1] E. Wilson, Metal Sci. 18 (1984) 471–484.

[2] K. Ishida, J. Alloys Comp. 220 (1995) 126–131.

[3] S. Neelakantan, P. Rivera-Díaz-del-Castillo, S. van der Zwaag, Scripta Mater. 60 (2009) 611–614.

[4] R. Bauer, E. Jägle, W. Baumann, E. Mittemeijer, Phil. Mag. 91 (2011) 437–457.

[5] G. Krauss, Steels: Processing, structure and performance, ASM international, 2005.

[6] M. Umemoto, E. Yoshitake, I. Tamura, J. Mater. Sci. 18 (1983) 2893–2904.

[7] S. Banerjee, P. Mukhopadhyay, Phase transformations: Examples from titanium and zirconium alloys, Pergamon Materials Series, 2007.

[8] H. Bhadeshia, R. Honeycombe, Steels: Microstructure and properties, Butterworth-Heinemann, 2006.

[9] W. Burgers, Physica 1 (1934) 561–586.

[10] M. Bönisch, T. Waitz, M. Calin, W. Strotzki, J. Eckert, Int. J. Plas. 85 (2016) 190–202.

[11] S. Mahajan, M. Green, D. Brasen, Metall. Trans. A 8 (1977) 283–293.

[12] J. Singh, S. Ranganathan, Phys. State. Sol. 73 (1981) 243–248.

[13] C. Cayron, Acta Mater. 69 (2015) 189–202.

[14] P. Toledo, G. Krexner, M. Prem, H. Weber, V. Dmitriev, Phys. Rev. B 64 (2001) 114104.

[15] K. Hermann, Crystallography and surface structure, Wiley-VCH, 2011.

[16] C. Chu, H. Huang, P. Kao, D. Gan, Scripta Metall. 30 (1994) 505–508.

[17] Centre D'information Du Cobalt, Cobalt monograph, Battelle Memorial Institute, 1960.

[18] B. Levinger, Trans. AIME 197 (1953) 195.

[19] H. Bhadeshia, Acta Metall. 29 (1981) 1117.

[20] V. Raghavan, D. Antia, Metall. Trans. A 27 (1996) 1127–1132.

[21] A. Borgenstam, M. Hillert, Acta Mater. 5 (1997) 2079–2091.

[22] S. Cotes, A. Fernández Guillermet, M. Sade, J. Alloy Comp. 280 (1998) 168–177.

[23] M. Balumbo, CALPHAD 32 (2008) 693–708.

[24] A. Stormvinter, A. Borgenstam, J. Agren, Metall. Mater. Trans A 43 (2012) 3870–3879.

[25] G. Ghosh, G. Olson, Acta Metall. Mater. 42 (1994) 3361–3370.

[26] G. Ghosh, G. Olson, Acta Metall. Mater. 42 (1994) 3371–3379.

[27] J. Eshelby, J. Appl. Phys. 25 (1954) 255.

[28] W. Cai, R. Sills, D. Barnett, W. Nix, J. Mech. Phys. Sol. 66 (2014) 154–171.

[29] J. Hirth, J. Lothe, Theory of dislocations, Wiley Interscience Publication, 1982.

[30] D. Lide, CRC Handbook of Chemistry and Physics, CRC Press, 2008.

[31] G. Ghosh, G. Olson, Acta Mater. 50 (2002) 2655–2675.

[32] Z. Trojanová, P. Maksimiyuk, P. Lukáč, Phys. Stat. Sol. 143 (1994) 75–77.

[33] R. Rao, A. Ramanand, J. Low Temp. Whys. 26 (1977) 365–377.

[34] I. Toda-Caraballo, E. Galindo-Nava, P. Rivera-Díaz-del-Castillo, J. Alloys Comp. 566 (2013) 217–228.

[35] J. Eshelby, Prog. Solid Mech. 2 (1961) 89–140.

[36] E. Galindo-Nava, P. Rivera-Díaz-del-Castillo, Acta Mater. 98 (2015) 81–83.

[37] X. Guan, Y. Nishizawa, K. Okamura, H. Numakura, M. Koiwa, Mater. Sci. Eng. A 370 (2004) 73–77.

[38] H. Sawada, K. Kawakami, M. Sugiyama, Mater. Trans. 46 (2005) 1140–1147.

[39] P. Marinelli, A. Baruj, S. Cotes, A. Fernández Guillermet, M. Sade, Mater. Sci. Eng. A 273 (1999) 498–502.

[40] Y. Imai, T. Murata, M. Nakamoto, Nitrogen-alloyed steels: fundamentals and applications, Agne Gijutsu Center, 1997.

[41] Z. Cai, D. Tang, H. Jiang, S. Zhao, L. Hui, J. Iron Steel Res. Int. 15 (2008) 82–85.

[42] S. Nayak, R. Anumolu, R. Misra, K. Kim, D. Lee, Mater. Sci. Eng. A 498 (2008) 442–456.

[43] S. van Bohemen, Mater. Sci. Tech. 28 (2012) 1487–1495.

[44] J. Tobata, K. Ngo-Huynh, N. Nakada, T. Tsuchiyama, S. Takaki, ISIJ Int. 52 (2012) 1377–1382.

[45] Y. Toji, H. MAtsuda, M. Herbig, P. Choi, D. Raabe, Acta Mater. 65 (2014) 215–228.

[46] R. Davis, J. Mater. Sci. 14 (1979) 712–722.

[47] M. Bönisch, M. Calin, T. Waitz, A. Panigrahi, M. Zehetbauer, A. Gebert, W. Skrotzki, J. Eckert, Sci. Technol. Adv. Mater. 14 (2013) 055004.

[48] S. Jonsson, Metall. Mater. Trans. B 29 (1988) 361–370.

[49] G. Olson, M. Cohen, Scripta Metall. 9 (1975) 1247–1254.

[50] G. Olson, M. Cohen, Scripta Metall. 11 (1977) 345–347.

[51] V. Boyko, R. Garber, A. Kossevich, Reversible crystal plasticity, Springer, 1994.

[52] B. Nikon, N. Shevchenko, T. Sizova, A. Babkevich, Scripta Metall. 21 (1987) 1169–1774.

[53] H. Shin, S. Lee, J. Jun, C. Choi, Mater. Sci. Tech. 18 (2002) 429–432.

[54] T. Omori, W. Ito, K. Ando, K. Oikawa, R. Kainuma, K. Ishida, Mater. Trans. 47 (2006) 2377–2380.

[55] Y. Liu, H. Yang, Y. Liu, B. Jiang, J. Ding, R. Woodward, Acta Mater. 53 (2005) 3625–3634.